

# Neutrino Flavor Transformation in Neutron Star Mergers

Yi Qiu<sup>1,2</sup>, David Radice<sup>1,2,3</sup>, Sherwood Richers<sup>4</sup>, and Maitraya Bhattacharyya<sup>1,2</sup>

<sup>1</sup> *Institute for Gravitation and the Cosmos, The Pennsylvania State University, University Park PA 16802, USA*

<sup>2</sup> *Department of Physics, The Pennsylvania State University, University Park PA 16802, USA*

<sup>3</sup> *Department of Astronomy & Astrophysics, The Pennsylvania State University, University Park PA 16802, USA and*

<sup>4</sup> *Department of Physics & Astronomy, University of Tennessee Knoxville, Knoxville TN 37996, USA*

We present the first numerical relativity simulations including neutrino flavor transformations that could result from flavor instabilities, quantum many-body effects, or potential beyond standard model physics in neutron star mergers. We find that neutrino flavor transformations impact the composition and structure of the remnant, potentially leaving an imprint on the post-merger gravitational-wave signal. They also have a significant impact on the composition and nucleosynthesis yields of the ejecta.

*Introduction.*—Multi-messenger astronomy is entering an exciting new era, with cutting-edge detectors set to observe gravitational waves (GWs) and their electromagnetic counterparts from compact object mergers at unprecedented rates [1–13]. This advancement promises to shed light on some of the most profound questions in astrophysics, particularly regarding the nature of dense matter in neutron stars [14–17]. While observations of kilonovae have confirmed that binary neutron star (BNS) mergers are a site of rapid neutron-capture (r-process) enrichment [18–21], the exact yields and detailed composition of the ejecta remain uncertain [22–25]. These uncertainties stem from the complex interplay of nuclear physics, neutrino interactions [26, 27], and the hydrodynamical evolution of the merger remnant [28]. In particular, neutrino flavor oscillations, which alter the electron fraction ( $Y_e$ ) of the outflows, play a crucial role in shaping the conditions for r-process element synthesis [29–33].

Accurate modeling of these complex phenomena requires not only solving general relativistic magnetohydrodynamics (GRMHD) equations but also implementing a comprehensive scheme to evolve the neutrino radiation transport [34–38]. In numerical simulations, modeling neutrino transport typically requires solving a 7-dimensional Boltzmann equation to capture their evolution in both coordinate and phase space. However, this approach remains computationally infeasible due to its exorbitant cost [39, 40]. As a result, alternative methods such as the nondeterministic Monte Carlo approach [41] and approximate schemes like truncated moment methods [42–48] are commonly employed [49, 50].

So far, binary neutron star merger simulations have neglected neutrino flavor conversions. Based on the neutrino distributions from simulations without flavor transformation, the flavor evolution under neutrino-neutrino interactions [37, 51–64] can occur on nanosecond timescales, which are orders of magnitude shorter than the timescales of hydrodynamic evolution, making them unfeasible to capture on the fly [65, 66]. Important exceptions are the studies of post-merger accretion disks [31–33]. However, they considered only the evolution of disks around compact objects and did not consider the merger

phase itself, which is the most dynamical phase of the binary evolution and that sets the disk initial structure and composition [67]. Additionally, there have been works on the effects of neutrino flavor conversions in the context of core-collapse supernovae [68–70], and substantial discussion regarding the outcomes of fast flavor conversions using either radiation-only simulations [71–78], or analyzing static snapshots from classical hydrodynamical simulations [79–83].

In this *Letter*, we consider, for the first time, the impact of rapid, lepton number-preserving neutrino-flavor equilibration that could result from quantum many-body interactions [84], beyond standard model physics [85], or flavor instabilities [59] in neutron star mergers. We show that neutrino flavor transformation can impact the structure and composition of the remnant, possibly leaving detectable changes in the post-merger GW emission. Flavor transformation has a profound impact on the ejecta composition and associated nucleosynthesis yields, with relative isobaric abundances of some nuclear species changing by up to one order of magnitude.

*Setup.*—We model neutrino-flavor transformation using a Bhatnagar-Gross-Krook (BGK) collisional operator [86, 87],  $\frac{1}{\tau_a}(f^a - f)$ , which models flavor conversion as a relaxation towards an asymptotic equilibrium state. In the previous equation,  $\tau_a$  is the relaxation time,  $f$  is the neutrino distribution function, and  $f^a$  denotes  $f$  at its asymptotic mixing equilibrium state. Motivated by [84], we determine the mixing equilibrium states assuming detailed balance for neutrino many-body interactions, that is the neutrino number densities are chosen such that the reactions  $\nu_e \bar{\nu}_e \rightleftharpoons \nu_\mu \bar{\nu}_\mu \rightleftharpoons \nu_\tau \bar{\nu}_\tau$  are in equilibrium. Since only 4 neutrino species are considered, i.e.  $\nu_e, \nu_x, \bar{\nu}_e, \bar{\nu}_x$ , where  $x$  stands for  $\mu$  and  $\tau$  (anti-)neutrinos combined, the assumption yields  $N_e^a N_e^a = \frac{1}{4} N_x^a N_x^a$ , where  $N$  is the number densities of neutrinos.

We perform BNS merger simulations with THC\_M1 [48, 88–90]. Our code evolves the (lab frame) neutrino number density  $N$ , energy  $E$  and flux  $F^\alpha$  using conservation equations in the 3+1 form (see in [48]), where on the right hand side we add the BGK flavor conversion operators using the corresponding relaxation times and calculated

equilibrium values<sup>1</sup>. For this work, we adopt the closure prescription described in Sec. of the Supplemental Material. The neutrino mixing operators are implemented in an operator-split fashion.

We construct initial data assuming non-rotating equal-mass neutron stars with mass  $1.35M_{\odot}$  and an initial separation of 45 km, corresponding to  $\sim 3$ – $4$  orbits prior to merger, using the Lorene pseudo-spectral code [91]. Neutron star matter is described using the DD2 equation of state [92, 93]. We employ 7 levels of adaptive mesh refinement [94, 95] using the Carpet driver [96, 97] of the Einstein Toolkit [98, 99]. The inner-most refinement level covers each star prior to merger, as well as the central part of the merger remnant. We present three sets of simulations, i) no neutrino mixing (**No-Mixing**), ii) neutrino mixing with density threshold  $10^{11} \text{ g/cm}^3$  ( $\rho - 11$ ) and iii) neutrino mixing with density threshold  $10^{13} \text{ g/cm}^3$  ( $\rho - 13$ ). All simulations were conducted with both low resolution (LR) and standard resolution (SR), where the finest grid have spacing of  $h = 0.167 M_{\odot} \simeq 246 \text{ m}$  and  $0.125 M_{\odot} \simeq 184 \text{ m}$ , respectively. We discuss the SR results in the text. The LR results agree qualitatively, see Supplemental Material for more information. Similar to [68, 69], in the  $\rho - 11$  ( $\rho - 13$ ) simulations, we use uniform relaxation times  $\tau_a = 0.4 \text{ ns}^2$  for regions where the rest mass density  $\rho$  is below  $10^{11} \text{ g/cm}^3$  ( $10^{13} \text{ g/cm}^3$ ), and infinite relaxation times when  $\rho$  is above the threshold. The  $\rho - 13$  model is chosen because  $10^{13} \text{ g/cm}^3$  is roughly the density of the surface of the remnant [100], inside which the interaction with matter should dominate over the flavor conversion effects. The  $\rho - 11$  model considers a case in which flavor transformations become important only in the optically thin region, below density  $10^{11} \text{ g/cm}^3$ .

*Results.*— Our simulations start from the late inspiral phase of the BNS, the stars merge  $\sim 15$  ms from the beginning of the simulation. Since DD2 is a stiff equation of state the remnants are stable against gravitational collapse. We evolve the system for an additional  $\sim 30$  ms post-merger to be able to capture the bulk of the dynamical mass ejection. In Fig. 1, we show the distribution of electron fractions, rest mass densities, electron neutrino and heavy lepton neutrino number densities on the x-y and x-z planes for the  $\rho - 11$  and the **No-Mixing** simulations. These snapshots, taken at  $\sim 15$  ms post-merger, capture the general dynamics of the remnant disk. In the equatorial plane and lower angle polar regions, we observe that the electron fraction of the ac-

cretion disk surrounding the merger remnant is substantially lower in the  $\rho - 11$  case than that in the **No-Mixing** simulation. In addition, as the electron (anti-)neutrinos undergoing  $\nu_e, \bar{\nu}_e \rightarrow \nu_x, \bar{\nu}_x$  flavor conversions, we find electron neutrinos to be less abundant in the outer disk (i.e.,  $\rho < 10^{11} \text{ g/cm}^3$ ) in the  $\rho - 11$  simulation than the **No-Mixing** simulation. Heavy lepton neutrinos exhibit the opposite trend.

We compute the remnant binding energies in Fig. 2, by integrating the GW energy losses. The  $\rho - 13$  simulation has the highest GW luminosity and the most bound remnant, followed by the  $\rho - 11$  simulation, and then the least in the **No-Mixing** simulation. In particular, the binding energies for the  $\rho - 13$  remnants are  $\sim 20\%$  greater than the **No-Mixing** remnants. Consistently, we find that these remnant have higher maximum density and smaller central value of the lapse function, as shown in the Supplementary Material. This could be the result of the enhanced thermal and electron (anti-)neutrino losses in the outer layers of these remnant favored by neutrino flavor transformation. We remark that a similar effect was recently reported by [85] in the context of core-collapse supernovae. This result suggests that gravitational wave observations could, at least in principle, constrain the physics of neutrino flavor transformation. We have also analyzed the post-merger GW spectra and found evidence of a shift in the peak frequency of the post-merger signal as a result of mixing (see Supplemental Material). However, we could not resolve this trend in the lower-resolution simulations, so we cannot conclusively rule out that it is a numerical artifact.

To quantify the ejecta properties, we measure the flux of unbound material satisfying the geodesic criterion at a sphere located at  $\sim 200M_{\odot}$  (295 km) away from the center of the simulation domain. Fig. 3 compares the electron fraction profiles and nucleosynthesis yields for the three models. Due to the flavor conversions from electron neutrinos to heavy lepton neutrinos, the induced deficits of electron neutrinos lead to a decrease in the neutrino reabsorption  $\nu_e + n \rightarrow p + e^-$ . Therefore, the mixing simulations have more neutron-rich ( $Y_e < 0.2$ ) materials in the ejecta, with the  $\rho - 11$  simulation having the most, followed by  $\rho - 13$  simulation, and the **No-Mixing** simulation the least. The  $\rho - 11$  simulation generates up to 5 times more neutron-rich ejecta than the **No-Mixing** simulation, while  $\rho - 13$  simulation produces up to twice as much. Both differences significantly exceed the reported  $10\% - 30\%$  numerical errors estimated from comparisons between M1 and Monte Carlo neutrino transport schemes [49, 101]. The lower panel of Fig. 3 presents the corresponding nucleosynthesis yields, calculated using the convolution method as in our previous work [27, 102]. Due to the strong dependence of r-process nucleosynthesis on the ejecta  $Y_e$ , we observe an order-of-magnitude difference in lanthanide and heavy element production between the  $\rho - 11$  and the **No-Mixing** sim-

<sup>1</sup> Note that the mixing equilibrium states of  $E$  and  $F^{\alpha}$  are determined by both the balance for neutrino number densities and energy conservations in the fluid frame.

<sup>2</sup> A sub-nano second relaxation time is chosen to show that our scheme is capable of considering neutrino oscillations at fast flavor conversion timescale.

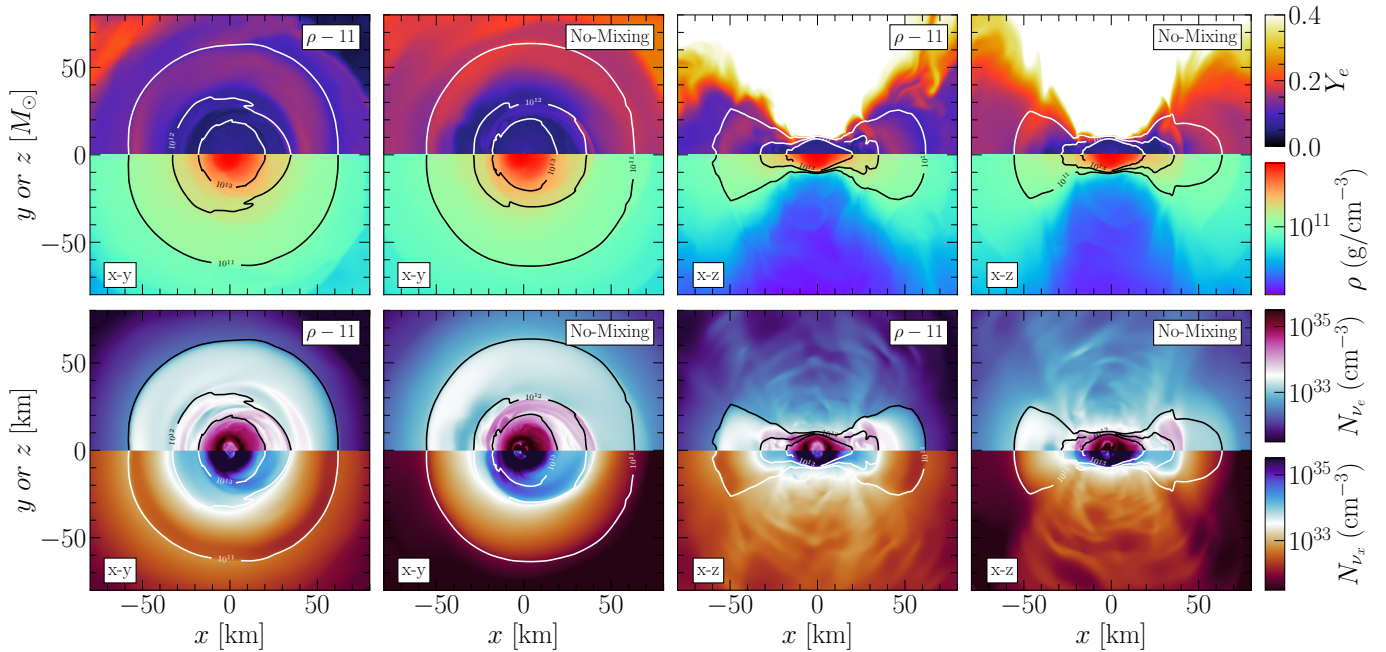


Figure 1. Simulation snapshots in the equatorial: x-y (meridional: x-z) planes for the  $\rho - 11$  and the **No-Mixing** models at  $\sim 15$  ms after merger on the left (right) four panels, respectively. The top-row panels show electron fractions (upper half) and rest mass densities (lower half). The second-row panels display electron neutrino number densities (upper half) and heavy lepton neutrino number densities (lower half). The contour lines denote where the density is at  $10^{11}$ ,  $10^{12}$  and  $10^{13}$  g/cm $^3$ . We find that after merger, the disk in the  $\rho - 11$  mixing model is more neutron rich than that of the **No-Mixing** model. Due to flavor conversion effects transforming electron (anti-)neutrinos to heavy lepton neutrinos, we also find that electron neutrinos are more abundant in the **No-Mixing** than the  $\rho - 11$ , and vice versa for heavy lepton neutrinos.

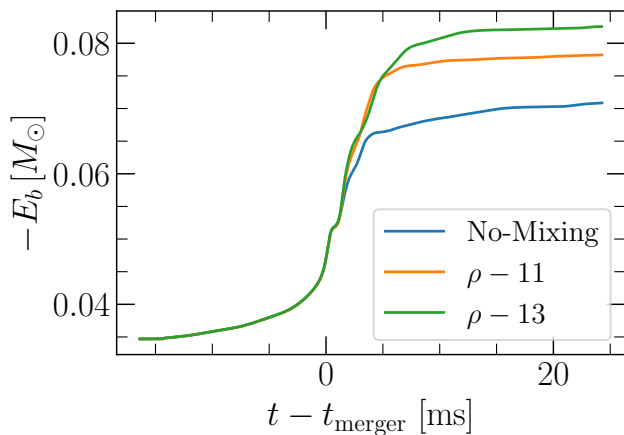


Figure 2. The evolution of the gravitational binding energy in the three models. The  $\rho - 13$  remnant is the most bound, followed by the  $\rho - 11$  simulation, and then by the **No-Mixing** simulation. Notably, the binding energy for the  $\rho - 13$  remnant is  $\sim 20\%$  greater than the **No-Mixing** remnant.

ulations, and a factor of two between the  $\rho - 13$  and the **No-Mixing** simulations. Notably, the differences caused by flavor conversion effects range from approximately 200% to 1000%.

Furthermore, we find that changing the neutrino mix-

ing conditions give rise to quantitatively different ejecta properties. In the  $\rho - 13$  simulation, the mixing is turned on in the inner disk where density is between  $10^{11}$  g/cm $^3$  and  $10^{13}$  g/cm $^3$ . In this region, electron (anti-)neutrinos remain in thermal equilibrium with the medium while undergoing flavor conversion to heavy lepton neutrinos. The latter can freely propagate outward. Once these heavy lepton neutrinos reach the outer disk where the density is below  $10^{11}$  g/cm $^3$ , a sufficient amount of them convert back into electron neutrinos, leading to an excess of electron neutrinos compared to the  $\rho - 11$  simulation. Therefore, as shown in 3, the  $\rho - 13$  simulation yields up to 3 times less neutron-rich ejecta, and correspondingly fewer heavy elements than the  $\rho - 11$  simulation.

Such effects are further illustrated in Fig. 4, which shows the ratio of electron neutrino absorption rates,  $\lambda_{\nu_e}$  between the  $\rho - 11$  and the  $\rho - 13$  simulations. In neutron-rich ejecta, the electron neutrino absorption rate is approximately proportional to the electron fraction equilibration rate [10, 11, 18]

$$\frac{dY_e}{dt} = \lambda_{\nu_e} (1 - Y_e) - \lambda_{\bar{\nu}_e} Y_e \approx \lambda_{\nu_e}. \quad (1)$$

In the outer disk where density is below  $10^{11}$  g/cm $^3$ , the electron neutrino absorption rate is significantly higher in  $\rho - 13$  simulation than those of the  $\rho - 11$  simulation,

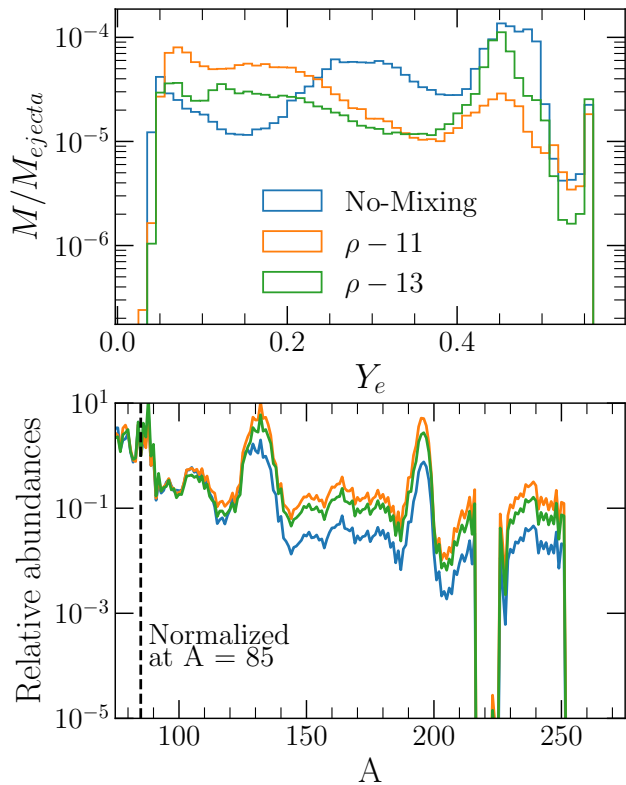


Figure 3. Upper panel: histograms of the electron fraction distributions of the ejecta. Due to neutrino mixing, the ejecta are generally more neutron rich in the  $\rho - 11$  simulation and the  $\rho - 13$  simulation than that in the **No-Mixing** simulation. The  $\rho - 11$  simulation has the most low ( $< 0.1$ )  $Y_e$  material in the ejecta, followed by  $\rho - 13$  simulation, and then by the **No-Mixing** simulation. Lower panel: the relative abundances of nuclei of mass number  $A$  formed in the ejecta. We normalize the yields at  $A = 85$ . Note that the yields for lanthanides and heavy elements are one order of magnitude higher in the  $\rho - 11$  simulation than the **No-Mixing** simulation. Because the yields are determined by the r-process, which will be enhanced/suppressed by more/less neutron-rich ejecta, the ranking between the three models is consistent as the electron fraction histograms.

leading to a more rapid increase in  $Y_e$  for the corresponding ejecta. This explains why we see up to 3 times less neutron-rich ejecta, and up to 2 times less heavy element produced in the  $\rho - 13$  simulation.

*Conclusion.*—We report on the first numerical relativity simulations including the dynamical effects of lepton number-preserving neutrino flavor equilibration that could be driven by quantum many-body effects, beyond standard-model physics, or flavor instabilities. Our study demonstrates that such transformations can impact the structure and composition of the merger remnant and of its accretion disk. At high densities, the conversion of electron-type neutrinos and anti-neutrinos into heavy-lepton neutrinos accelerates the contraction of the outer

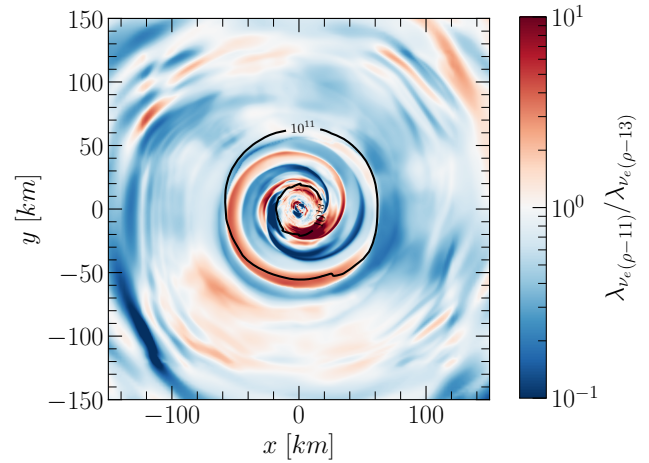


Figure 4. Ratio of the electron neutrino absorption rates for the  $\rho - 11$  simulation over the  $\rho - 13$  simulation on the x-y plane, taken at  $\sim 15$  ms after merger. The contours are drawn for rest mass density of  $10^{11}$  and  $10^{13}$  g/cm $^3$ . We see greater electron neutrino absorption rates in the  $\rho - 13$  simulation than those of the  $\rho - 11$  simulation for the outer disk region where density is below  $10^{11}$  g/cm $^3$ .

layers of the remnant. This is manifested by a significant increase, of up to  $\sim 20\%$ , in the overall postmerger GW luminosity, which could be probed with future GW experiments, such as Cosmic Explorer [103] and the Einstein Telescope [104]. At lower densities, the depletion of electron-type neutrinos due to flavor conversion results in more neutron rich ejecta and boosts the production of heavy r-process elements with  $A \gtrsim 120$  by up to one order of magnitude.

Interestingly, not only whether or not neutrino flavor transformation occurs, but also *where* it occurs has a strong impact on the nucleosynthesis. In particular, we examine two density-dependent neutrino mixing models where neutrino flavor conversions are considered everywhere with density below either  $10^{11}$  or  $10^{13}$  g/cm $^3$ . While both cases have significantly more neutron rich ejecta and higher abundances of heavy r-process elements than the **No-Mixing** runs, there are important differences between them. In particular, if neutrinos undergo flavor transformation within the disk, e.g., at densities between  $10^{11}$  and  $10^{13}$  g/cm $^3$ , this boosts the neutrino losses from the disk, because the disk is optically thin to heavy lepton-neutrinos. Some of the escaping neutrinos are then converted back to electron-type neutrinos and absorbed into the ejecta, decreasing the average  $Y_e$  and  $\langle A \rangle$  of the ejecta.

Future work will extend this work by exploring mixing prescriptions motivated by the fast-flavor instability [70, 105] and considering a broader range of equations of states and merger outcomes. We also aim to include muonic interactions [106, 107] and neutrino-lepton inelastic scatterings and pair processes [108, 109].



It is our pleasure to acknowledge Joseph Carlson, Gail McLaughlin, and Albino Perego for discussions during various stages of development of this work. DR, SR, and MB thank the Institute for Nuclear Theory at the University of Washington for the kind hospitality during the INT-23-2 program, during which this project was conceived. This research was supported in part by the INT's U.S. Department of Energy grant No. DE-FG02-00ER41132. YQ and MB were supported by the U.S. Department of Energy, Office of Science, Division of Nuclear Physics under Award Number(s) DE-SC0021177 and DE-SC0024388 DR acknowledges support from the Sloan Foundation, from the National Science Foundation under Grants No. PHY-2020275, AST-2108467, PHY-2116686, and PHY-2407681. SR acknowledges support from the National Science Foundation under Grant No. PHY-2412683. Simulations were performed on TACC's Frontera (NSF LRAC allocation PHY23001), on NERSC's Perlmutter, and on the Pennsylvania State University's Institute for Computational and Data Sciences' Roar supercomputer. This research used resources of the National Energy Research Scientific Computing Center, a DOE Office of Science User Facility supported by the Office of Science of the U.S. Department of Energy under Contract No. DE-AC02-05CH11231.

- 
- [1] B. P. Abbott *et al.* (LIGO Scientific, Virgo), *Phys. Rev. Lett.* **116**, 061102 (2016), arXiv:1602.03837 [gr-qc].
- [2] B. P. Abbott *et al.* (LIGO Scientific, Virgo), *Phys. Rev. Lett.* **119**, 161101 (2017), arXiv:1710.05832 [gr-qc].
- [3] B. P. Abbott *et al.* (LIGO Scientific, Virgo, Fermi-GBM, INTEGRAL), *Astrophys. J. Lett.* **848**, L13 (2017), arXiv:1710.05834 [astro-ph.HE].
- [4] B. P. Abbott *et al.* (KAGRA, LIGO Scientific, Virgo), *Living Rev. Rel.* **19**, 1 (2016), arXiv:1304.0670 [gr-qc].
- [5] D. Eichler, M. Livio, T. Piran, and D. N. Schramm, *Nature* **340**, 126 (1989).
- [6] D. Radice, S. Bernuzzi, and A. Perego, *Ann. Rev. Nucl. Part. Sci.* **70**, 95 (2020), arXiv:2002.03863 [astro-ph.HE].
- [7] A. Perego, D. Radice, and S. Bernuzzi, *Astrophys. J. Lett.* **850**, L37 (2017), arXiv:1711.03982 [astro-ph.HE].
- [8] M. Ruffert and H. T. Janka, *Astron. Astrophys.* **344**, 573 (1999), arXiv:astro-ph/9809280.
- [9] O. Just, M. Obergaulinger, H. T. Janka, A. Bauswein, and N. Schwarz, *Astrophys. J. Lett.* **816**, L30 (2016), arXiv:1510.04288 [astro-ph.HE].
- [10] M. Cusinato, F. M. Guercilena, A. Perego, D. Logoteta, D. Radice, S. Bernuzzi, and S. Ansoldi, (2021), 10.1140/epja/s10050-022-00743-5, arXiv:2111.13005 [astro-ph.HE].
- [11] D. Martin, A. Perego, W. Kastaun, and A. Arcones, *Class. Quant. Grav.* **35**, 034001 (2018), arXiv:1710.04900 [astro-ph.HE].
- [12] M. Diamond, D. F. G. Fiorillo, G. Marques-Tavares, I. Tamborra, and E. Vitagliano, *Phys. Rev. Lett.* **132**, 101004 (2024), arXiv:2305.10327 [hep-ph].
- [13] A. Vigna-Gómez *et al.*, *Phys. Rev. Lett.* **132**, 191403 (2024), arXiv:2310.01509 [astro-ph.HE].
- [14] L. Baiotti and L. Rezzolla, *Rept. Prog. Phys.* **80**, 096901 (2017), arXiv:1607.03540 [gr-qc].
- [15] G. Baym, T. Hatsuda, T. Kojo, P. D. Powell, Y. Song, and T. Takatsuka, *Rept. Prog. Phys.* **81**, 056902 (2018), arXiv:1707.04966 [astro-ph.HE].
- [16] G. F. Burgio, H. J. Schulze, I. Vidana, and J. B. Wei, *Prog. Part. Nucl. Phys.* **120**, 103879 (2021), arXiv:2105.03747 [nucl-th].
- [17] H. T. Janka, (2025), arXiv:2502.14836 [astro-ph.HE].
- [18] Y. Z. Qian and S. E. Woosley, *Astrophys. J.* **471**, 331 (1996), arXiv:astro-ph/9611094.
- [19] R. D. Hoffman, S. E. Woosley, and Y. Z. Qian, *Astrophys. J.* **482**, 951 (1997), arXiv:astro-ph/9611097.
- [20] M.-R. Wu, R. Fernández, G. Martínez-Pinedo, and B. D. Metzger, *Mon. Not. Roy. Astron. Soc.* **463**, 2323 (2016), arXiv:1607.05290 [astro-ph.HE].
- [21] A. B. Balantekin, M. J. Cervia, A. V. Patwardhan, R. Surman, and X. Wang, *Astrophys. J.* **967**, 146 (2024), arXiv:2311.02562 [astro-ph.HE].
- [22] D. Kasen, B. Metzger, J. Barnes, E. Quataert, and E. Ramirez-Ruiz, *Nature* **551**, 80 (2017), arXiv:1710.05463 [astro-ph.HE].
- [23] S. Wanajo, Y. Sekiguchi, N. Nishimura, K. Kiuchi, K. Kyutoku, and M. Shibata, *Astrophys. J. Lett.* **789**, L39 (2014), arXiv:1402.7317 [astro-ph.SR].
- [24] Y. L. Zhu, K. Lund, J. Barnes, T. M. Sprouse, N. Vassh, G. C. McLaughlin, M. R. Mumpower, and R. Surman, *Astrophys. J.* **906**, 94 (2021), arXiv:2010.03668 [astro-ph.HE].
- [25] J. Barnes, Y. L. Zhu, K. A. Lund, T. M. Sprouse, N. Vassh, G. C. McLaughlin, M. R. Mumpower, and R. Surman, *Astrophys. J.* **918**, 44 (2021), arXiv:2010.11182 [astro-ph.HE].
- [26] P. L. Espino, P. Hammond, D. Radice, S. Bernuzzi, R. Gamba, F. Zappa, L. F. Longo Micchi, and A. Perego, *Phys. Rev. Lett.* **132**, 211001 (2024), arXiv:2311.00031 [astro-ph.HE].
- [27] P. L. Espino, D. Radice, F. Zappa, R. Gamba, and S. Bernuzzi, *Phys. Rev. D* **109**, 103027 (2024), arXiv:2311.12923 [astro-ph.HE].
- [28] P. L. Espino, G. Bozzola, and V. Paschalidis, *Phys. Rev. D* **107**, 104059 (2023), arXiv:2210.13481 [gr-qc].
- [29] Y.-L. Zhu, A. Perego, and G. C. McLaughlin, *Phys. Rev. D* **94**, 105006 (2016), arXiv:1607.04671 [hep-ph].
- [30] M.-R. Wu, I. Tamborra, O. Just, and H.-T. Janka, *Phys. Rev. D* **96**, 123015 (2017), arXiv:1711.00477 [astro-ph.HE].
- [31] X. Li and D. M. Siegel, *Phys. Rev. Lett.* **126**, 251101 (2021), arXiv:2103.02616 [astro-ph.HE].
- [32] O. Just, S. Abbar, M.-R. Wu, I. Tamborra, H.-T. Janka, and F. Capozzi, *Phys. Rev. D* **105**, 083024 (2022), arXiv:2203.16559 [astro-ph.HE].
- [33] R. Fernández, S. Richers, N. Mulyk, and S. Fahlman, *Phys. Rev. D* **106**, 103003 (2022), arXiv:2207.10680 [astro-ph.HE].
- [34] S. Rosswog, M. Liebendoerfer, F. K. Thielemann, M. B. Davies, W. Benz, and T. Piran, *Astron. Astrophys.* **341**, 499 (1999), arXiv:astro-ph/9811367.
- [35] F. Foucart, *Liv. Rev. Comput. Astrophys.* **9**, 1 (2023), arXiv:2209.02538 [astro-ph.HE].
- [36] C. E. Collins, A. Bauswein, S. A. Sim, V. Vijayan, G. Martínez-Pinedo, O. Just, L. J. Shingles, and

- M. Kromer, *Mon. Not. Roy. Astron. Soc.* **521**, 1858 (2023), [arXiv:2209.05246 \[astro-ph.HE\]](#).
- [37] M. C. Volpe, *Rev. Mod. Phys.* **96**, 025004 (2024), [arXiv:2301.11814 \[hep-ph\]](#).
- [38] K. Kawaguchi, S. Fujibayashi, and M. Shibata, *Phys. Rev. D* **111**, 023015 (2025), [arXiv:2410.02380 \[astro-ph.HE\]](#).
- [39] K. Sumiyoshi, S. Fujibayashi, Y. Sekiguchi, and M. Shibata, *Astrophys. J.* **907**, 92 (2021), [arXiv:2010.10865 \[astro-ph.HE\]](#).
- [40] M. K. Bhattacharyya and D. Radice, (2022), [10.1016/j.jcp.2023.112365](#), [arXiv:2212.01409 \[math.NA\]](#).
- [41] F. Foucart, *Mon. Not. Roy. Astron. Soc.* **475**, 4186 (2018), [arXiv:1708.08452 \[astro-ph.HE\]](#).
- [42] K. S. Thorne, *Mon. Not. Roy. Astron. Soc.* **194**, 439 (1981).
- [43] M. Shibata, K. Kiuchi, Y.-i. Sekiguchi, and Y. Suwa, *Prog. Theor. Phys.* **125**, 1255 (2011), [arXiv:1104.3937 \[astro-ph.HE\]](#).
- [44] C. Y. Cardall, E. Endeve, and A. Mezzacappa, *Phys. Rev. D* **88**, 023011 (2013), [arXiv:1305.0037 \[astro-ph.HE\]](#).
- [45] F. Foucart, E. O'Connor, L. Roberts, L. E. Kidder, H. P. Pfeiffer, and M. A. Scheel, *Phys. Rev. D* **94**, 123016 (2016), [arXiv:1607.07450 \[astro-ph.HE\]](#).
- [46] Y. Sekiguchi, K. Kiuchi, K. Kyutoku, and M. Shibata, *Phys. Rev. D* **91**, 064059 (2015), [arXiv:1502.06660 \[astro-ph.HE\]](#).
- [47] Y. Sekiguchi, K. Kiuchi, K. Kyutoku, M. Shibata, and K. Taniguchi, *Phys. Rev. D* **93**, 124046 (2016), [arXiv:1603.01918 \[astro-ph.HE\]](#).
- [48] D. Radice, S. Bernuzzi, A. Perego, and R. Haas, *Mon. Not. Roy. Astron. Soc.* **512**, 1499 (2022), [arXiv:2111.14858 \[astro-ph.HE\]](#).
- [49] F. Foucart, P. C.-K. Cheong, M. D. Duez, L. E. Kidder, H. P. Pfeiffer, and M. A. Scheel, *Phys. Rev. D* **110**, 083028 (2024), [arXiv:2407.15989 \[astro-ph.HE\]](#).
- [50] P. C.-K. Cheong, F. Foucart, M. D. Duez, A. Offermans, N. Muhammed, and P. Chawhan, *Astrophys. J.* **975**, 116 (2024), [arXiv:2407.16017 \[astro-ph.HE\]](#).
- [51] G. Sigl and G. Raffelt, *Nucl. Phys. B* **406**, 423 (1993).
- [52] R. F. Sawyer, *Phys. Rev. D* **72**, 045003 (2005), [arXiv:hep-ph/0503013](#).
- [53] H. Duan, G. M. Fuller, and Y.-Z. Qian, *Phys. Rev. D* **74**, 123004 (2006), [arXiv:astro-ph/0511275](#).
- [54] I. Izaguirre, G. Raffelt, and I. Tamborra, *Phys. Rev. Lett.* **118**, 021101 (2017), [arXiv:1610.01612 \[hep-ph\]](#).
- [55] S. Chakraborty, R. S. Hansen, I. Izaguirre, and G. Raffelt, *JCAP* **03**, 042 (2016), [arXiv:1602.00698 \[hep-ph\]](#).
- [56] F. Capozzi, B. Dasgupta, E. Lisi, A. Marrone, and A. Mirizzi, *Phys. Rev. D* **96**, 043016 (2017), [arXiv:1706.03360 \[hep-ph\]](#).
- [57] S. Richers, D. Willcox, and N. Ford, *Phys. Rev. D* **104**, 103023 (2021), [arXiv:2109.08631 \[astro-ph.HE\]](#).
- [58] T. Morinaga, *Phys. Rev. D* **105**, L101301 (2022), [arXiv:2103.15267 \[hep-ph\]](#).
- [59] S. Richers and M. Sen, "Fast Flavor Transformations," in *Handbook of Nuclear Physics*, edited by I. Tanihata, H. Toki, and T. Kajino (2022) pp. 1–17, [arXiv:2207.03561 \[astro-ph.HE\]](#).
- [60] M.-R. Wu, M. George, C.-Y. Lin, and Z. Xiong, *Phys. Rev. D* **104**, 103003 (2021), [arXiv:2108.09886 \[hep-ph\]](#).
- [61] H. Nagakura, L. Johns, A. Burrows, and G. M. Fuller, *Phys. Rev. D* **104**, 083025 (2021), [arXiv:2108.07281 \[astro-ph.HE\]](#).
- [62] F. Capozzi and N. Saviano, *Universe* **8**, 94 (2022), [arXiv:2202.02494 \[hep-ph\]](#).
- [63] S. Abbar and H. Nagakura, *Phys. Rev. D* **109**, 023033 (2024), [arXiv:2310.03807 \[astro-ph.HE\]](#).
- [64] M. Zaizen and H. Nagakura, *Phys. Rev. D* **109**, 083031 (2024), [arXiv:2311.13842 \[astro-ph.HE\]](#).
- [65] L. Johns, (2023), [arXiv:2306.14982 \[hep-ph\]](#).
- [66] L. Johns, (2024), [arXiv:2401.15247 \[astro-ph.HE\]](#).
- [67] A. Camilletti, A. Perego, F. M. Guercilena, S. Bernuzzi, and D. Radice, *Phys. Rev. D* **109**, 063023 (2024), [arXiv:2401.04102 \[astro-ph.HE\]](#).
- [68] J. Ehring, S. Abbar, H.-T. Janka, G. Raffelt, and I. Tamborra, *Phys. Rev. D* **107**, 103034 (2023), [arXiv:2301.11938 \[astro-ph.HE\]](#).
- [69] J. Ehring, S. Abbar, H.-T. Janka, G. Raffelt, and I. Tamborra, *Phys. Rev. Lett.* **131**, 061401 (2023), [arXiv:2305.11207 \[astro-ph.HE\]](#).
- [70] T. Wang and A. Burrows, (2025), [arXiv:2503.04896 \[astro-ph.HE\]](#).
- [71] Z. Xiong, M.-R. Wu, S. Abbar, S. Bhattacharyya, M. George, and C.-Y. Lin, *Phys. Rev. D* **108**, 063003 (2023), [arXiv:2307.11129 \[astro-ph.HE\]](#).
- [72] D. F. G. Fiorillo and G. G. Raffelt, *Phys. Rev. Lett.* **133**, 221004 (2024), [arXiv:2403.12189 \[hep-ph\]](#).
- [73] Z. Xiong, M.-R. Wu, M. George, and C.-Y. Lin, *Phys. Rev. Lett.* **134**, 051003 (2025), [arXiv:2403.17269 \[astro-ph.HE\]](#).
- [74] A. Kost, L. Johns, and H. Duan, *Phys. Rev. D* **109**, 103037 (2024), [arXiv:2402.05022 \[hep-ph\]](#).
- [75] J. Liu, H. Nagakura, M. Zaizen, L. Johns, R. Akaho, and S. Yamada, *Phys. Rev. D* **111**, 023051 (2025), [arXiv:2411.08503 \[astro-ph.HE\]](#).
- [76] J. P. Kneller, J. Froustey, E. B. Grohs, F. Foucart, G. C. McLaughlin, and S. Richers, (2024), [arXiv:2410.00719 \[hep-ph\]](#).
- [77] D. Lacroix, A. Bauge, B. Yilmaz, M. Mangin-Brinet, A. Roggero, and A. B. Balantekin, *Phys. Rev. D* **110**, 103027 (2024), [arXiv:2409.20215 \[hep-ph\]](#).
- [78] H. Nagakura, M. Zaizen, J. Liu, and L. Johns, *Phys. Rev. D* **111**, 043028 (2025), [arXiv:2501.14145 \[astro-ph.HE\]](#).
- [79] S. Richers, *Phys. Rev. D* **106**, 083005 (2022), [Erratum: *Phys. Rev. D* **109**, 129901 (2024)], [arXiv:2206.08444 \[astro-ph.HE\]](#).
- [80] E. Grohs, S. Richers, S. M. Couch, F. Foucart, J. P. Kneller, and G. C. McLaughlin, *Phys. Lett. B* **846**, 138210 (2023), [arXiv:2207.02214 \[hep-ph\]](#).
- [81] J. Froustey, S. Richers, E. Grohs, S. D. Flynn, F. Foucart, J. P. Kneller, and G. C. McLaughlin, *Phys. Rev. D* **109**, 043046 (2024), [arXiv:2311.11968 \[astro-ph.HE\]](#).
- [82] E. Grohs, S. Richers, S. M. Couch, F. Foucart, J. Froustey, J. P. Kneller, and G. C. McLaughlin, *Astrophys. J.* **963**, 11 (2024), [arXiv:2309.00972 \[astro-ph.HE\]](#).
- [83] E. Grohs, S. Richers, J. Froustey, F. Foucart, J. P. Kneller, and G. C. McLaughlin, (2025), [arXiv:2501.07540 \[astro-ph.HE\]](#).
- [84] J. D. Martin, D. Neill, A. Roggero, H. Duan, and J. Carlson, *Phys. Rev. D* **108**, 123010 (2023), [arXiv:2307.16793 \[hep-ph\]](#).
- [85] J. Ehring, S. Abbar, H. T. Janka, G. Raffelt, K. Nakamura, and K. Kotake, (2024), [arXiv:2412.02750 \[astro-](#)

- ph.HE].
- [86] P. L. Bhatnagar, E. P. Gross, and M. Krook, *Phys. Rev.* **94**, 511 (1954).
- [87] H. Nagakura, L. Johns, and M. Zaizen, *Phys. Rev. D* **109**, 083013 (2024), arXiv:2312.16285 [astro-ph.HE].
- [88] D. Radice and L. Rezzolla, *Astron. Astrophys.* **547**, A26 (2012), arXiv:1206.6502 [astro-ph.IM].
- [89] D. Radice, L. Rezzolla, and F. Galeazzi, *Mon. Not. Roy. Astron. Soc.* **437**, L46 (2014), arXiv:1306.6052 [gr-qc].
- [90] D. Radice, L. Rezzolla, and F. Galeazzi, *Class. Quant. Grav.* **31**, 075012 (2014), arXiv:1312.5004 [gr-qc].
- [91] E.ourgoulhon, P. Grandclement, K. Taniguchi, J.-A. Marck, and S. Bonazzola, *Phys. Rev. D* **63**, 064029 (2001), arXiv:gr-qc/0007028.
- [92] S. Typel, G. Ropke, T. Klahn, D. Blaschke, and H. H. Wolter, *Phys. Rev. C* **81**, 015803 (2010), arXiv:0908.2344 [nucl-th].
- [93] M. Hempel and J. Schaffner-Bielich, *Nucl. Phys. A* **837**, 210 (2010), arXiv:0911.4073 [nucl-th].
- [94] M. J. Berger and J. Olinger, *J. Comput. Phys.* **53**, 484 (1984).
- [95] M. Berger and P. Colella, *J. Comput. Phys.* **82**, 64 (1989).
- [96] E. Schnetter, S. H. Hawley, and I. Hawke, *Class. Quant. Grav.* **21**, 1465 (2004), arXiv:gr-qc/0310042.
- [97] C. Reisswig, R. Haas, C. D. Ott, E. Abdikamalov, P. Mösta, D. Pollney, and E. Schnetter, *Phys. Rev. D* **87**, 064023 (2013), arXiv:1212.1191 [astro-ph.HE].
- [98] F. Löffler *et al.*, *Class. Quant. Grav.* **29**, 115001 (2012), arXiv:1111.3344 [gr-qc].
- [99] R. Haas, M. Rizzo, D. Boyer, S. R. Brandt, P. Diener, D. Garzon, L. T. Sanches, B.-J. Tsao, S. Cupp, Z. Etienne, T. P. Jacques, L. Ji, E. Schnetter, L. Wernicke, M. Alcubierre, D. Alic, G. Allen, M. Ansorg, F. G. L. Armengol, M. Babiuc-Hamilton, L. Baiotti, W. Bengert, E. Bentivegna, S. Bernuzzi, K. Bhatia, T. Bode, G. Bozzola, B. Brendal, B. Bruegmann, M. Campanelli, M. Chabanov, C.-H. Cheng, F. Cipolletta, G. Corvino, R. D. Pietri, A. Dima, H. Dimmelmeier, J. Doherty, R. Dooley, N. Dorband, M. Eley, Y. E. Khamra, L. Ennoggi, J. Faber, G. Ficarra, T. Font, J. Frieben, B. Giacomazzo, T. Goodale, C. Gundlach, I. Hawke, S. Hawley, I. Hinder, E. A. Huerta, S. Husa, T. Ikeda, S. Iyer, D. Johnson, A. V. Joshi, J. Kalinani, A. Kankani, W. Kastaun, T. Kellermann, A. Knapp, M. Koppitz, P. Laguna, G. Lanferman, P. Lasky, F. Löffler, H. Macpherson, I. Markin, J. Masso, L. Menger, A. Merzky, J. M. Miller, M. Miller, P. Moesta, P. Montero, B. Mundim, P. Nelson, A. Nerozzi, S. C. Noble, C. Ott, L. J. Papenfort, R. Paruchuri, M. Pirog, D. Pollney, D. Price, D. Radice, T. Radke, C. Reisswig, L. Rezzolla, C. B. Richards, D. Rideout, M. Ripeanu, L. Sala, J. A. Schewtschenko, B. Schutz, E. Seidel, E. Seidel, J. Shalf, S. Shankar, K. Sible, U. Sperhake, N. Stergioulas, W.-M. Suen, B. Szilagy, R. Takahashi, M. Thomas, J. Thornburg, C. Tian, W. Tichy, M. Tobias, A. Tonita, S. Tootle, P. Walker, M.-B. Wan, B. Wardell, H. Witek, M. Zilhão, B. Zink, and Y. Zlochower, “The einstein toolkit,” (2024).
- [100] M. Hanauske, K. Takami, L. Bovard, L. Rezzolla, J. A. Font, F. Galeazzi, and H. Stöcker, *Phys. Rev. D* **96**, 043004 (2017), arXiv:1611.07152 [gr-qc].
- [101] F. Foucart, M. D. Duez, F. Hebert, L. E. Kidder, H. P. Pfeiffer, and M. A. Scheel, *Astrophys. J. Lett.* **902**, L27 (2020), arXiv:2008.08089 [astro-ph.HE].
- [102] D. Radice, A. Perego, K. Hotokezaka, S. A. Fromm, S. Bernuzzi, and L. F. Roberts, *Astrophys. J.* **869**, 130 (2018), arXiv:1809.11161 [astro-ph.HE].
- [103] D. Reitze *et al.*, *Bull. Am. Astron. Soc.* **51**, 035 (2019), arXiv:1907.04833 [astro-ph.IM].
- [104] M. Punturo *et al.*, *Class. Quant. Grav.* **27**, 194002 (2010).
- [105] S. Abbar, M.-R. Wu, and Z. Xiong, *Phys. Rev. D* **109**, 083019 (2024), arXiv:2401.17424 [astro-ph.HE].
- [106] H. H.-Y. Ng, C. Musolino, S. D. Tootle, and L. Rezzolla, (2024), arXiv:2411.19178 [astro-ph.HE].
- [107] M. A. Pajkos and E. R. Most, *Phys. Rev. D* **111**, 043013 (2025), arXiv:2409.09147 [astro-ph.HE].
- [108] P. C.-K. Cheong, F. Foucart, H. H.-Y. Ng, A. Offermans, M. D. Duez, N. Muhammed, and P. Chawhan, *Phys. Rev. D* **111**, 043036 (2025), arXiv:2410.20681 [astro-ph.HE].
- [109] L. Chiesa, M. Bhattacharyya, F. Mazzini, F. M. Guercilena, A. Perego, and D. Radice, (2024), arXiv:2412.04570 [astro-ph.HE].
- [110] G. N. Minerbo, *Journal of Quantitative Spectroscopy and Radiative Transfer* **20**, 541 (1978).
- [111] L. M. Murchikova, E. Abdikamalov, and T. Urbatsch, *Mon. Not. Roy. Astron. Soc.* **469**, 1725 (2017), arXiv:1701.07027 [astro-ph.HE].

## SUPPLEMENTAL MATERIAL

### The *THC\_M1* Scheme

In *THC\_M1*, we decompose the (neutrino) radiation stress energy tensors as

$$T_{\text{rad}}^{\alpha\beta} = En^\alpha n^\beta + F^\alpha n^\beta + n^\alpha F^\beta + P^{\alpha\beta}, \quad (2)$$

where  $n^\alpha$  is the future-oriented unit vector normal to the constant time hypersurfaces. The decomposition also gives  $P^{\alpha\beta}$ , the radiation pressure tensor, as the second order moment. In order to close the  $E$  and  $F^\alpha$  equations, we need to relate  $P^{\alpha\beta}$  with  $E$  and  $F^\alpha$ . A standard prescription is to use an analytic closure to express the neutrino radiation pressure in different optical depth regimes [43]

$$P_{\alpha\beta} = \frac{3\chi - 1}{2} P_{\alpha\beta}^{\text{thin}} + \frac{3(1 - \chi)}{2} P_{\alpha\beta}^{\text{thick}}, \quad (3)$$

where  $\chi \in [\frac{1}{3}, 1]$  is the Eddington factor. Using Minerbo closure [110], we express  $\chi$  as

$$\chi(\xi) = \frac{1}{3} + \xi^2 \left( \frac{6 - 2\xi + 6\xi^2}{15} \right), \quad \xi^2 = \frac{\tilde{F}_\alpha \tilde{F}^\alpha}{\tilde{E}^2} \quad (4)$$

where the  $\tilde{\cdot}$  quantities are the radiation fields in the fluid co-moving frame. In this work, we use the following ansatz for  $P^{\text{thick}}$

$$\tilde{P}_{\alpha\beta}^{\text{thick}} = \frac{1}{3} \tilde{E} (g_{\alpha\beta} + u_\alpha u_\beta) \quad (5)$$

where  $u^\alpha$  is the fluid four-velocity,  $g_{\alpha\beta}$  is the spacetime metric. In addition, we use

$$P_{\alpha\beta}^{\text{thin}} = \frac{F_\alpha F_\beta}{E} \quad (6)$$

in the optically thin limit [43, 111].

### Additional Diagnostics

In the top panel of Fig. 5 we show the minimum lapse as a function of time for the *No-Mixing*, the  $\rho - 11$ , and the  $\rho - 13$  simulations. As a consequence of our choice of a stiff equation of state, we see stable post-merger remnants for all simulations. Since remnant central density is inversely correlated with the minimum lapse, we find that the  $\rho - 13$  simulation remnant is the most compact, followed by  $\rho - 11$  simulation, with the *No-Mixing* case being the least compact. Their relative differences are more than 5%. This trend is further confirmed by the evolution of the maximum density,  $\rho_{\text{max}}$ , as shown in bottom panel of Fig. 5. The ranking of compactness, the  $\rho - 13$  simulation, followed by  $\rho - 11$  simulation, and then the *No-Mixing* simulation, is consistent in both diagnostics.

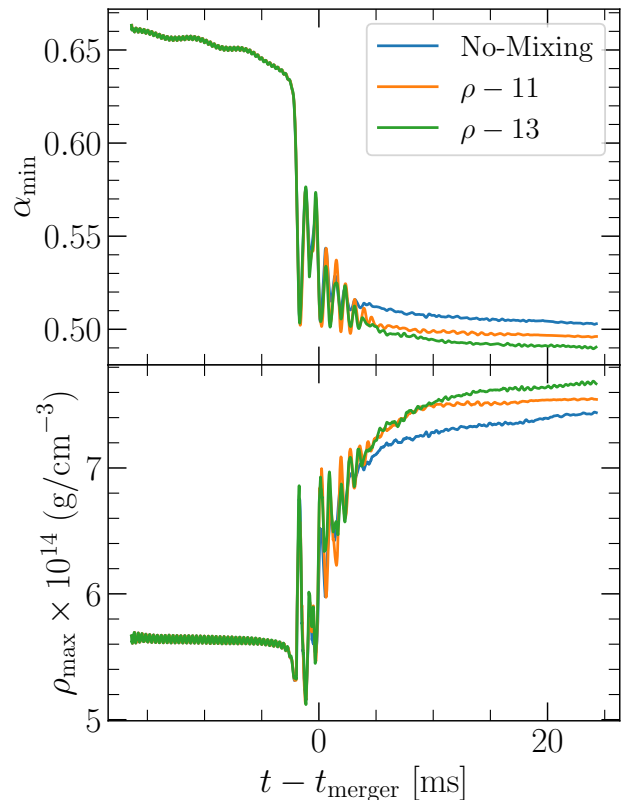


Figure 5. The evolutions of the minimum lapse (upper), and maximum density (lower) in the three models. The remnant NSs become stable at  $\sim 10$  ms after merger, we see the highest compactness in the  $\rho - 13$  simulation, then the  $\rho - 11$  simulation, and the least compact remnant in the *No-Mixing* simulation. The relative differences between different models are within 5%.

This may be due to the flavor swapping induced electron (anti-)neutrino losses in the outer layers of the remnant.

We keep track of the neutrino fluxes passing through a sphere of  $\sim 295$  km radius from the center of simulation domain and integrate them to obtain for–overall and individual flavors–neutrino luminosities. As shown in Fig. 6, in post-merger phase, the total neutrino luminosities are highest in the  $\rho - 13$  simulation, with the other two simulations being qualitatively comparable. For individual species, we see  $\rho - 13$  simulation has up to 400% more heavy lepton neutrino luminosity than the *No-Mixing* simulation, and up to 100% more than the  $\rho - 11$  simulation. In contrast, the electron (anti-)neutrinos luminosities are down by up to 200% in the  $\rho - 11$  simulation compared to the *No-Mixing* simulation. The results suggest that flavor conversions of  $\nu_e, \bar{\nu}_e \rightarrow \nu_x, \bar{\nu}_x$  are significant enough to be observed. Moreover, the fact that different mixing conditions lead to different neutrino luminosities also suggest that *where* neutrino flavor conversions occur is crucial for relevant observations.

We also present GW power spectra for SR simulations



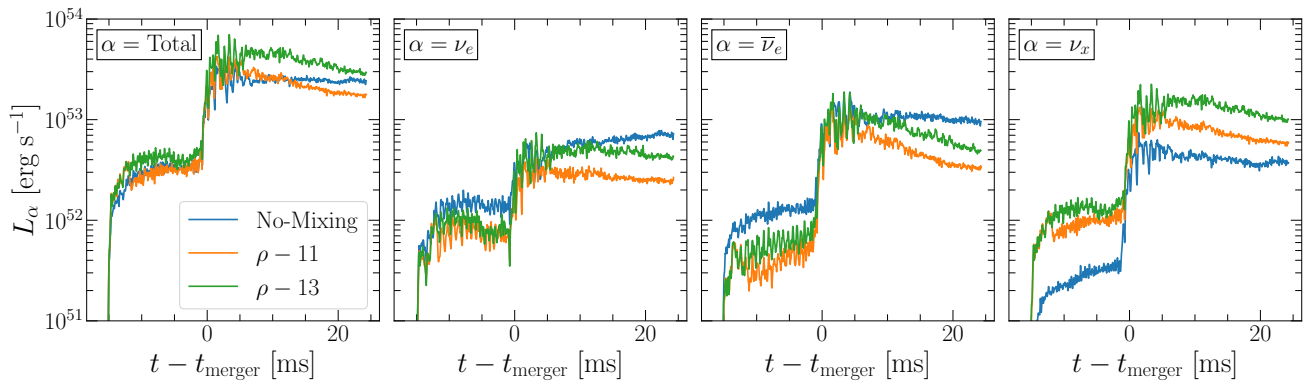


Figure 6. Neutrino luminosities evolutions for total,  $\nu_e$ ,  $\bar{\nu}_e$ , and  $\nu_x$ , respectively, in panels from left to right. Driven by the flavor conversions  $\nu_e, \bar{\nu}_e \rightarrow \nu_x, \bar{\nu}_x$ , we see that electron (anti-)neutrinos are more luminous in the **No-Mixing** simulation than the  $\rho - 11$  and the  $\rho - 13$  simulations, vice versa for heavy lepton neutrinos. Between two mixing models, the  $\rho - 13$  simulation has higher luminosities for all neutrino species compared to the  $\rho - 11$  simulation, which are due to the additionally enabled flavor conversion effects between  $10^{11} \text{g/cm}^3$  and  $10^{13} \text{g/cm}^3$  inner disk region.

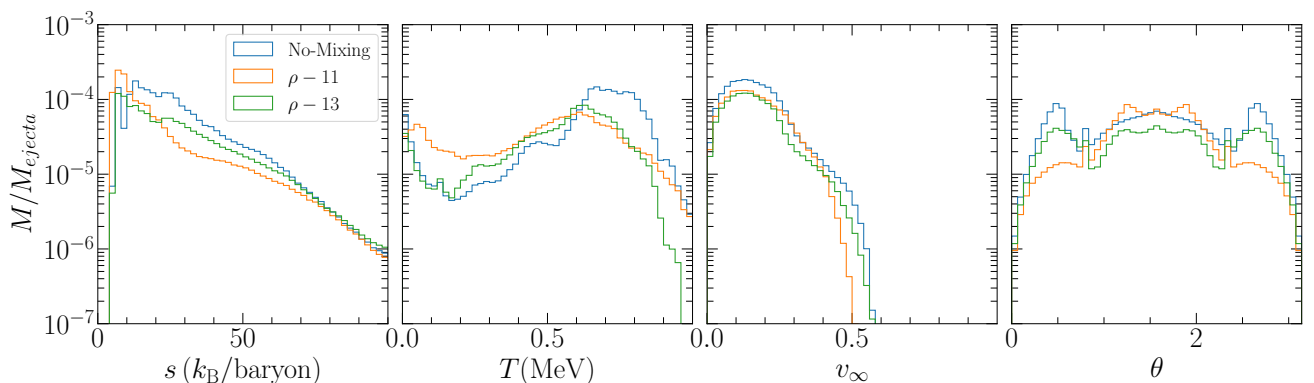


Figure 7. Histograms of the dynamical ejecta entropy, temperature, velocity at infinity and polar angle. The ejecta are observed on a sphere located at  $\sim 200M_\odot$  (295 km) away from the center of the simulation domain, based on geodesic criterion. The **No-Mixing** simulation, the  $\rho - 11$  simulation and the  $\rho - 13$  simulation ejecta are drawn in blue, orange and green, respectively. All diagnostics look similar in three models.

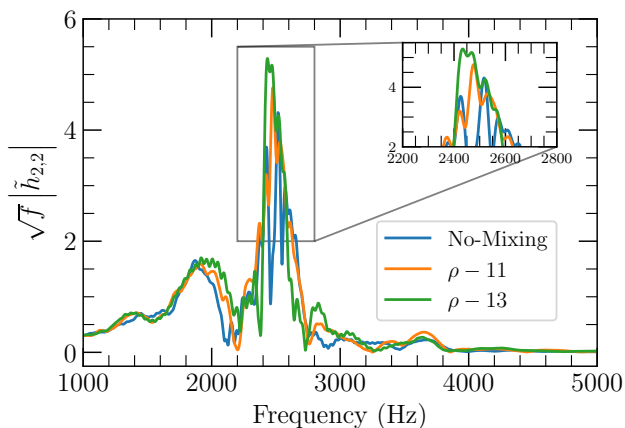


Figure 8. The GW spectra in the three models. The post-merger peak frequencies shift from high to lower in the **No-Mixing**, the  $\rho - 11$ , and the  $\rho - 13$  simulations. The difference between the peak frequency can be up to 100 Hz.

in Fig. 8. We find that the post-merger frequency peaks are different in the **No-Mixing** simulation, the  $\rho - 11$  simulation, and the  $\rho - 13$  simulation, with the discrepancy being up to 100 Hz. However, we note here that such frequency differences are subject to double-peak features as observed in the **No-Mixing** spectrum. Moreover, they can not be resolved in our LR runs, as such we cannot conclusively ruled out that these difference are due to finite resolution effects.

In addition to electron fraction, we also show in histograms of other relevant ejecta properties for SR simulations, including entropy, temperature, velocity at infinity and polar angle in the **No-Mixing**, the  $\rho - 11$ , and the  $\rho - 13$  models. The ejecta entropy distribution seems to be almost the same across the models, all peaked at  $\sim 10 k_B/\text{baryon}$ . Temperature and polar angle distributions have broad distributions. The ejecta velocities are lower than 0.5 in all simulations. In general, despite minor fluctuations due to numerical uncertainties, the overall

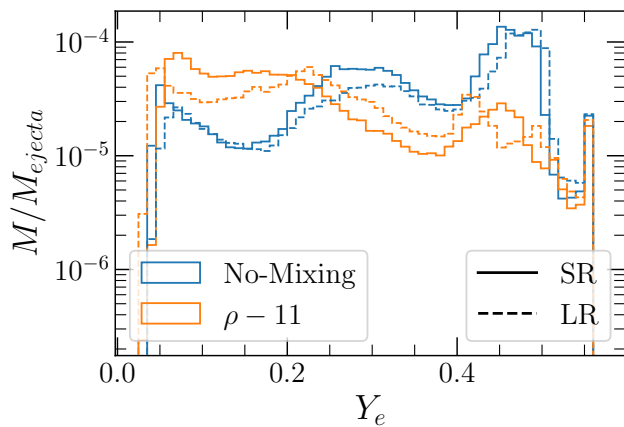


Figure 9. The electron fraction distributions of the dynamical ejecta in the **No-Mixing** and the  $\rho - 11$  simulations for both standard (solid) and low (dashed) resolutions. We see in both LR and SR that, the ejecta is generally neutron-richer in the  $\rho - 11$  simulation than that in the **No-Mixing** simulation, showing good consistency against resolutions.

properties of the ejecta, other than  $Y_e$ , are similar across our simulations.

#### *Finite-Resolution Effects*

As a consistency test, we compare the electron fraction profiles of the dynamical ejecta in Fig. 9 for the **No-Mixing** and the  $\rho - 11$  models in different resolutions. We see qualitatively the same distributions for the  $Y_e$  in corresponding LR vs. SR comparisons. The relative difference in neutron-rich tails does not exceed 30% for the  $\rho - 11$  LR and SR simulations, while the **No-Mixing** LR and SR simulations show negligible differences as well.